

Cascade adaptive optics: contrast performance analysis of a two-stage controller by numerical simulations

Nelly Cerpa-Urra^{a,b,*}, Markus Kasper^a, Caroline Kulcsár^b, Henri-François Raynaud^b, Cedric Taïssir Heritier^a

^aEuropean Southern Observatory, Karl-Schwarzschild Str. 2, Garching bei München, Germany, 85748

^bUniversité Paris-Saclay, Institut d'Optique Graduate School, CNRS, Laboratoire Charles Fabry, 91127, Palaiseau, France

Abstract. The contrast performance of current eXtreme Adaptive Optics (XAO) systems can be improved by adding a second AO correction stage featuring its own wavefront sensor, deformable mirror and real-time controller. We develop a dynamical model for such a cascade AO (CAO) system with two stages each controlled by a standard integrator, and study its control properties. We study how such a configuration can improve an existing system without modifying the first stage. We analyze the CAO architecture in general and show how part of the disturbance is transferred from low to high temporal frequencies with a nefarious effect of the 2nd stage integrator overshoot, and suggest possible ways to mitigate this. We also carry out numerical simulations of the particular case of a 1st stage AO using a Shack-Hartmann wavefront sensor and a 2nd stage AO with a smaller deformable mirror running at a higher framerate to reduce temporal error. In this case, we demonstrate that the 2nd stage improves imaging contrast by one order of magnitude and shortens the decorrelation time of atmospheric turbulence speckles by even a greater factor. The results show that CAO presents a promising and relatively simple way to upgrade some existing XAO systems and achieve improved imaging contrasts fostering a large number of science case including the direct imaging of Exoplanets.

Keywords: Adaptive Optics, XAO, CAO, Speckle lifetime.

*Nelly Cerpa-Urra, ncerpaur@eso.org

1 Introduction

Since the first detection of an exoplanet around a main sequence star more than 20 years ago,¹ the hunt for exoplanets has been more than prolific. Thousands of exoplanets have been detected (<http://exoplanets.org/>) using mostly radial velocity and transit techniques, and providing valuable information on a number of basic planet parameters such as orbit, mass, size and density. High-contrast imaging (HCI) with adaptive optics (AO), however, provides direct images of exoplanets that can be analyzed spectroscopically to characterize their atmospheres. HCI aims at reducing the host star's light flux at the location of the exoplanet, thereby minimizing the photon noise, and maximizing the detection sensitivity. It potentially reduces the required observing time to detect a planet from orbital period(s) for the indirect methods, to just a few nights or even a few hours

(depending on the exoplanet's apparent flux and the measurement noise). Although more than 99% of the planets discovered so far have been found indirectly, HCI led to the discovery of several young giant planets at relatively large orbital separations,²⁻⁸ but extending the search space to lower mass and older exoplanets at smaller orbital separations has proved to be a challenge. In particular, HCI requires bigger telescopes and improved technologies (AO, coronagraphy, instrumentation) to boost contrast sensitivity at very small angular separations.

For optical and near-IR HCI, the AO-corrected residual halo stellar flux is the main source of measurement noise.⁹ In order to obtain great contrast sensitivity for exoplanet imaging at small angular separations, it is therefore crucial to minimize this residual halo which is typically dominated by the AO temporal delay at small angular separations.¹⁰ A straightforward approach to reduce the temporal delay would be to run the AO system faster at the expense of increased detector read-noise.

Ultra-fast AO systems for high-contrast imaging are under development at several observatories, using either a single-stage,¹¹ a woofer-tweeter^{12,13} or a cascade adaptive optics (CAO) system with two stages¹⁴⁻¹⁶ approach. In the latter case, a 2nd AO stage with its own deformable mirror (DM), wavefront sensor (WFS) and RTC is added to the instrument behind a 1st stage AO system. This 2nd stage only sees the residuals of the wavefront pre-flattened by the 1st stage and can therefore employ a DM with small actuator stroke. As the scientific interest is mostly at very small angular separations, the AO correction radius¹⁷ can be small, and the number of actuators of the 2nd stage's DM can be relatively low, leading to a compact design and moderate computational demands. These properties, and the possibility to develop and test the 2nd stage stand-alone and retrofit it to an already existing 1st stage, make this approach very attractive for upgrades of existing AO systems such as VLT-SPHERE¹⁸ or VLT-AOF.¹⁹

Besides running fast, predictive control presents another way to reduce the temporal error. Predictive controllers have been proposed in the literature in many different forms,²⁰⁻³³ and some on-sky tests have been performed.³⁴⁻³⁸ With the greatly increased processing power and bandwidth of modern computers, predictive control has been recently brought back into the focus of AO engineering with integration in operational systems.³⁹⁻⁴²

In this work, we rather follow a simple approach and propose a CAO system with two stages, where each stage is controlled by a classical integrator. We introduce the generic CAO in Sec. 2 and study its temporal and control properties. In section 3, we present numerical simulations of a particular CAO case for an 8-m class telescope. The 1st stage is assumed to feature a Shack-Hartmann WFS and a DM controlling about 800 modes and running at 1 kHz frame rate while the faster 4 kHz 2nd stage features a Pyramid WFS⁴³ and controls about 200 modes. This case roughly represents the considered upgrades of some VLT AO systems mentioned above.

We also analyze ways to optimize the integrator gains for both stages and how to best split the light between them. We demonstrate an improved low frequency rejection by CAO which also reduces the lifetime of atmospheric residual speckles and their noise contribution in long exposures. A comprehensive discussion of these results is provided in Sec. 3.3.

2 Two-stage CAO system: principle and control analysis

2.1 Principle and general hypotheses

The principle of the two-stage CAO system is illustrated in Fig. 1: a 1st stage corrects for the incoming turbulent phase, producing a residual phase that enters a faster 2nd stage. The residual phase at the output of this 2nd stage is sent to the science camera. The wavelengths of the two WFSs

may be different, and may be also different from that of the science camera. The nature of each WFS and their dimensions will be detailed when addressing performance evaluation in Sec. 3.2.

The advantages of this kind of system can be summed up in three main points: first, the 2nd stage can be connected to any other already existing system; this can be especially helpful by reducing downtime of existing instruments and improve implementation time. Second, a CAO system reduces the stroke needed by the 2nd stage DM to correct for low order aberrations. And at last, the 2nd stage system can be designed and installed without modifying the 1st stage RTC, which is beneficial when the budget available for an upgrade is not sufficient for a complete overhaul.

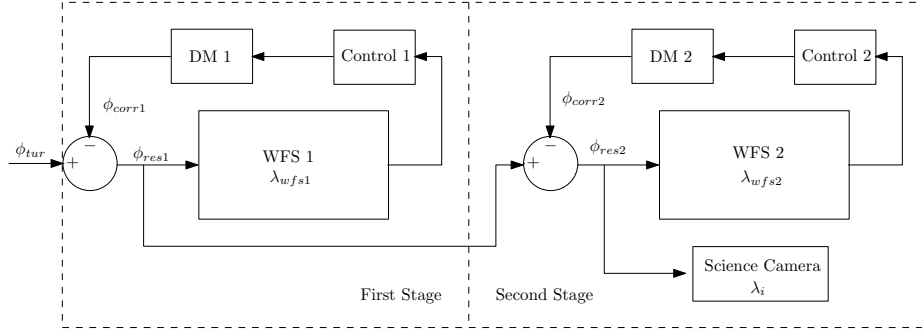


Fig 1 Two-stage CAO system architecture

Note that contrarily to standard CAO control, the 2nd stage (inner loop) is not seen by the 1st stage (outer loop), so that the stability of the inner and outer loops are sufficient to guarantee the stability of the CAO feedback. Each loop is controlled by an integral action controller (or integrator). Also, we will consider in the following that each WFS integrates the flux over one frame, T_1 for the 1st stage, T_2 for the 2nd stage, and that the two loop frequencies $F_1 = 1/T_1$ and $F_2 = 1/T_2$ are such that the 2nd stage frequency is a multiple of the 1st stage frequency, that is $F_2 = nF_1$, $n > 1$, $n \in \mathbb{N}$. Also, we suppose that each loop suffers a standard two-frame delay.

As each loop is controlled by an integrator, two natural questions arise: does this two-stage

CAO system behave like a double integrator in terms of rejection? And how to characterize the rejection for such a system with two different frame rates? The purpose of the next section is to address these questions thanks to a modal analysis.

2.2 Modal control analysis

In a standard AO loop, it is commonplace to analyse rejection by computing the frequency-domain response of the closed-loop controlled system. Once the frequency responses of the rejection transfer function (RTF) and noise propagation transfer function have been calculated, the effects on any incoming second-order stationary stochastic process with known power spectral density can be evaluated, allowing in particular to predict the expected value of the residual phase variance – see, Ref.⁴⁴ for the general case of linear controllers. These calculations rely on the hypothesis that the AO system is linear and time-invariant, so that to a given input frequency corresponds an output at the same frequency, albeit with possibly a different amplitude and nonzero phase shift.

This is no more true in the case of a two-stage CAO system featuring two different sampling frequencies, as the system loses its time invariance property. Take the case of an incoming disturbance which temporal spectrum contains energy between $F_1/2$ and $F_2/2$: this disturbance will be aliased by the 1st stage (with an attenuation due to the averaging by the WFS) at a frequency below $F_1/2$. In addition, the frequency range $[-F_1/2, F_1/2]$ will be periodized at period F_1 , which has to be accounted for at the 2nd stage level. Hence, one particular frequency of the turbulent phase entering the whole two-stage system will produce several frequencies at the output of the system, so that the linearity in the frequency domain is lost: the rejection transfer function cannot be evaluated anymore as a point-by-point ratio of the output and input spectra.

We propose to analyse the rejection and noise propagation produced by this system thanks to

a modal decomposition of the turbulent phase, leading to a simpler scalar temporal and frequency analysis on a single mode. All the simulations are carried out using MATLAB-SIMULINK with DMs and WFSs having unitary gains.

To illustrate the multi-rate effect, let us take a pure sine wave with frequency $f_0 < F_1/2$ entering the noise-free CAO system. The 1st stage produces a correction signal at loop frequency F_1 , and the continuous-time residual is averaged and up-sampled by the 2nd stage at loop frequency F_2 . The frequency support $\{-f_0, +f_0\}$ of our initial disturbance spectrum will thus be modified into a support of the form $\{\pm f_0 + mF_1\}$, $m \in \mathbb{Z}$. Figure 2-(a) shows the spectrum of the resulting signal at the output of the 2nd stage over the range $[-F_2/2, +F_2/2]$ for a pure sinusoidal signal of amplitude 1 and frequency $f_0 = 40$ Hz and loop frequencies $F_1 = 1$ kHz and $F_2 = 4$ kHz. The relative attenuation of the peaks at high frequency is due to the averaging filter convolution over T_2 which produces a sinc in the frequency domain. When $f_0 > F_1/2$, the resulting frequencies will be of the same form $\{\pm f_0 + mF_1\}$, $m \in \mathbb{Z}$, but only the aliased part of the signal will be corrected by the two stages, whereas the non-aliased part will only be corrected by the 2nd stage. This is illustrated in Fig. 2-(b), and explains the higher value at $\pm f_0$. It is thus clear that the theoretical evaluation of the rejection for any given spectrum needs to distinguish what is rejected by both stages and what is only rejected by the 2nd one.

To make this distinction, one can notice that any continuous-time signal ϕ^{tur} can simply be decomposed under the form

$$\phi^{\text{tur}}(t) = \phi^{\text{is}}(t) + \bar{\phi}_k^{\text{tur}} \text{ for } (k-1)T_1 \leq t < kT_1, \quad (1)$$

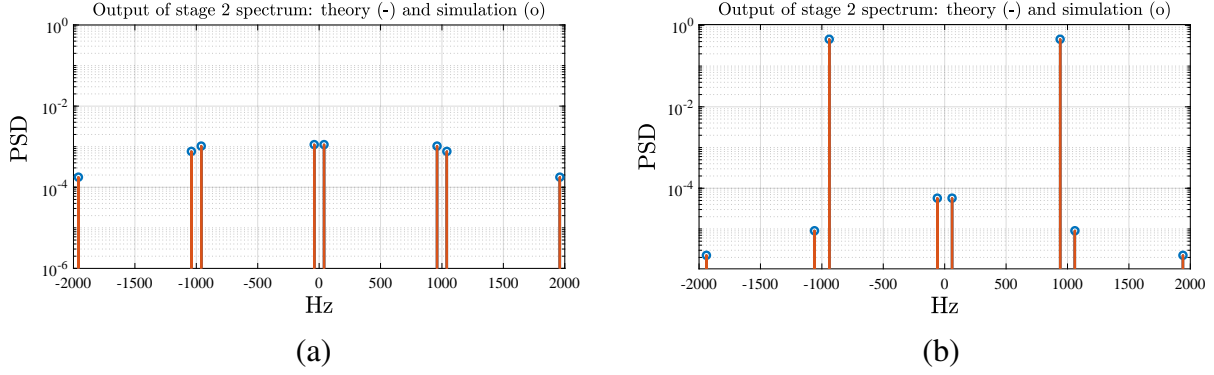


Fig 2 Illustration of spectrum periodization for an input sinusoidal signal at $f_0 = 40$ Hz (left) and of aliasing and periodization for an input sinusoidal signal at $f_0 = 940$ Hz (right). Loop frequencies are $F_1 = 1$ kHz and $F_2 = 4$ kHz. The red lines correspond to the theoretical calculations, the blue circles to the empirical power spectral density computed from the simulation data by non-averaged periodogram. The y-axis is in arbitrary units.

where $\phi^{\text{is}}(t) = \phi^{\text{tur}}(t) - \bar{\phi}_k^{\text{tur}}$ is the so-called the inter-sampling signal and $\bar{\phi}_k^{\text{tur}}$ is defined as

$$\bar{\phi}_k^{\text{tur}} = \frac{1}{T_1} \int_{(k-1)T_1}^{kT_1} \phi^{\text{tur}}(t) dt. \quad (2)$$

The inter-sampling signal ϕ^{is} is not affected by the 1st stage, only $\bar{\phi}_k^{\text{tur}}$ is. Therefore, the analysis can be conducted by combining three operations:

- compute $\bar{\phi}_k^{\text{tur}}$, the signal averaged and sampled at T_1 , to be rejected by the 1st stage running at F_1 ,
- compute ϕ^{is} , the inter-sampling signal to be compensated by the 2nd stage only at F_2 ,
- periodize the residual spectrum of the rejection of $\bar{\phi}_k^{\text{tur}}$ by the 1st stage at frequency F_1 on $[-F_2/2, F_2/2]$, in order to obtain the 1st stage residual $\bar{\phi}^{\text{res},1}$ which is to be compensated by the 2nd stage. The periodization is due to the upsampling at frequency F_2 , as $\bar{\phi}^{\text{res},1}$ is constant over T_1 and thus upsampled by repeating the same value F_2/F_1 times (effect of the 2nd stage zero-order hold).

The inter-sampling signal for the 2nd stage, obtained from ϕ^{is} using averages on T_2 , has not been considered as it is not affected by the 2nd stage.

The complete residual signal after 1st stage, namely $\phi^{\text{res},1} = \bar{\phi}^{\text{res},1} + \phi^{\text{is}}$, is compensated by the 2nd stage to give a residual signal denoted by $\phi^{\text{res},2}$. These various signals ϕ^{is} , $\bar{\phi}^{\text{res},1}$, $\phi^{\text{res},1}$ and $\phi^{\text{res},2}$ are shown in Fig. 3 for the 40 Hz sinusoid with amplitude 1 and for $F_1 = 1$ kHz and $F_2 = 4$ kHz. The inter-sampling signal ϕ^{is} (in green) plus the residual $\bar{\phi}^{\text{res},1}$ (in pink) gives the signal $\phi^{\text{res},1}$ (in blue) to be compensated by the 2nd stage. The residual signal $\phi^{\text{res},2}$ (in red) is obtained at the output of the 2nd stage. It can be noticed that the inter-sampling signal seems to have a similar energy to that of the residual $\phi^{\text{res},2}$.

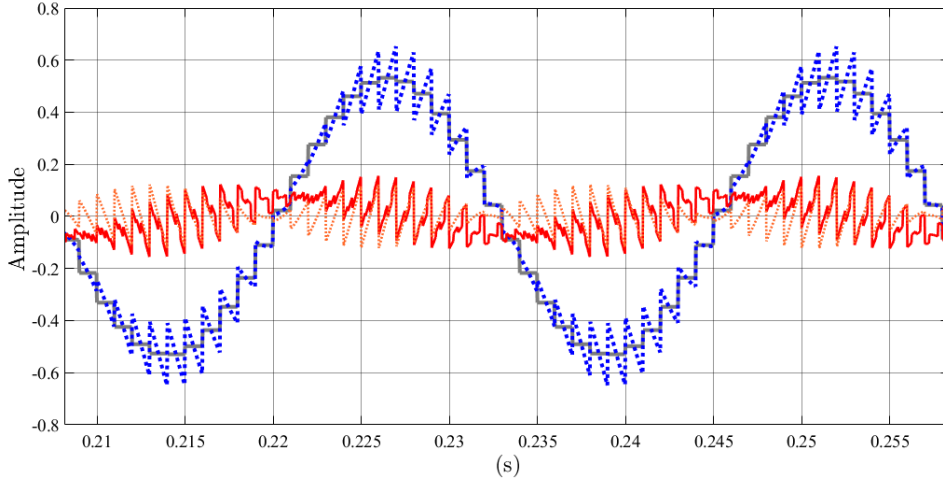


Fig 3 For an input sinusoidal signal of amplitude 1 at $f_0 = 40$ Hz: inter-sampling signal ϕ^{is} (dotted orange), residual $\bar{\phi}^{\text{res},1}$ (plain grey), 1st stage output $\phi^{\text{res},1}$ (dotted-dashed blue) and 2nd stage residual signal $\phi^{\text{res},2}$ (plain red). Loop frequencies are $F_1 = 1$ kHz and $F_2 = 4$ kHz. The y-axis is in arbitrary units.

The rejection does not affect all these signals in the same way: if we denote by R_1 and R_2 the rejection transfer functions (RTFs) of stages 1 and 2 respectively, and considering the decomposition in Eq. (1) and the explanations given above, the power spectral density (PSD) $S_{\text{res},2}$ of the

residual signal at the output of the 2nd stage will be given by

$$S_{\phi^{\text{res},2}}(e^{i\omega T_2}) = |R_2(e^{i\omega T_2})|^2 [S_{\phi^{\text{is}}}(e^{i\omega T_2}) + \text{III}(|R_1|^2 S_{\bar{\phi}^{\text{tur}}})(e^{i\omega T_2})] , \quad (3)$$

where $S_{\phi^{\text{is}}}$ and $S_{\bar{\phi}^{\text{tur}}}$ are respectively the PSDs of ϕ^{is} and $\bar{\phi}^{\text{tur}}$, and $\text{III}(G)$ is the periodized version of G with period F_1 on the interval $[-F_2/2, +F_2/2]$. In order to evaluate the rejection and compare it with a double integrator at F_2 , Fig. 4 displays the various RTFs that affect the signals passing through the system differently for $F_1 = 1$ kHz and $F_2 = 4$ kHz. The gains for the two integrators is 0.5, and the double integrator (with gain 0.0625) has been stabilized using a lead-lag term $1 + \alpha(1 - z^{-1})$ with $\alpha = 4$ in order to limit the frequency-domain overshoot. From Fig. 4, one can see that the two-stage CAO system will reject the low frequency content of a signal like a double integrator until about 100 Hz. However, the inter-sampling signal (which is only rejected by R_2) has a spectrum which spreads until high frequencies because of F_1 periodization. It will thus not be well attenuated by the 2nd stage and may even be amplified by the overshoot of the integrator. As for high-frequency and high-energy input signals above about 300 Hz, they are unlikely to be present in an atmospheric perturbation. The two-stage system is expected to have a better behavior in the range 180-300 Hz because it is well below the overshoot of the double integrator.

Let us take now the example of the temporal spectrum of a Zernike mode of radial order $n_{\text{rad}}=3$, with cut-off frequency $f_c = 0.3(n_{\text{rad}} + 1)V/D = 1.5$ Hz ($V = 10$ m/s, $D = 8$ m).⁴⁵ The schematic PSD, 2-stage residual PSD and double integrator residual PSD are plotted in Fig. 5-(a) for a case without measurement noise. The behavior of the 2-stage system is similar or better than that of the double integrator for the part of the spectrum until about 600 Hz. The inter-sampling signal produces the two peaks at high frequency, leading to a global variance that is above the

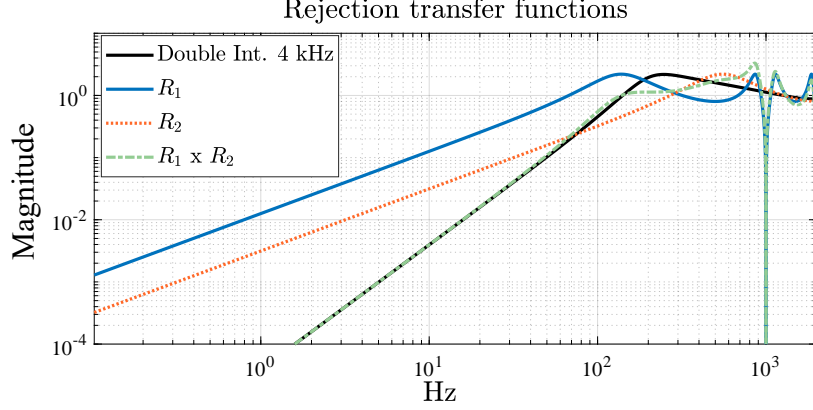


Fig 4 RTFs over the frequency range $[0, F_2/2]$. The signal $\bar{\phi}^{\text{tur}}$ generated at $F_1 = 1$ kHz and upsampled at $F_2 = 4$ kHz is rejected by $R_1 \times R_2$, while the inter-sampling signal ϕ^{is} is only rejected by R_2 . The double integrator RTF at $F_2 = 4$ kHz is in black. The y-axis is in arbitrary units.

double integrator. In Fig. 5-(b), it can be seen that the rejection of $\bar{\phi}^{\text{res},1}$ is to be improved at low frequencies, which is well done by the 2nd stage as shown with the CAO curve in Fig. 5-(a). The high frequencies of the inter-sampling signal ϕ^{is} stay almost identical after the 2nd stage as they are not attenuated, as noticed previously in the Fig. 3, and as it can also be seen in Fig. 4. The inter-sampling signal thus dominates the global signal in terms of variance, which can be computed using the formula in:²⁸

$$\text{Var}(\phi^{\text{is}}) \stackrel{\text{a.s.}}{=} \int_{-\infty}^{+\infty} (1 - |\text{sinc}(\pi f T_1)|^2) S_{\phi^{\text{tur}}}(f) df, \quad (4)$$

where $S_{\phi^{\text{tur}}}(f)$ is the PSD of $\phi^{\text{tur}}(t)$. For this schematic spectrum, with $\text{Var}(\phi^{\text{tur}}) = 3.4$ arbitrary units [arb. units] over $[-F_2/2, F_2/2]$, one finds $\text{Var}(\phi^{\text{is}}) \simeq 1.4 \cdot 10^{-5}$ [arb. unit] when the variance of the residual signal at the output of stage 2 is $\text{Var}(\phi^{\text{res},2}) \simeq 2 \cdot 10^{-5}$ [arb. unit]. The double integrator is of course lower with a residual variance of about $4 \cdot 10^{-8}$ [arb. unit].

When measurement noise is present, its propagation needs to be accounted for even in a very low noise situation, as shown in the following. The dimensioning of the 1st and 2nd stages leads to

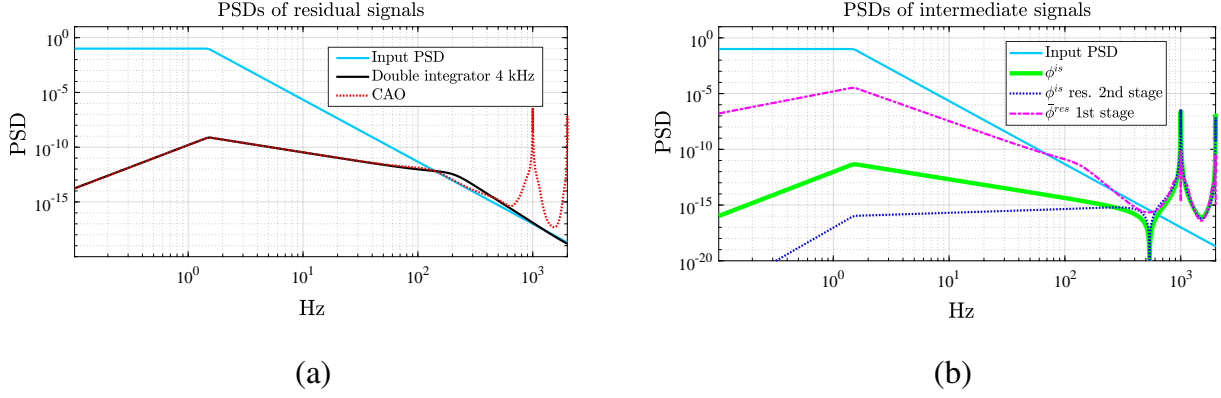


Fig 5 Theoretical PSDs: on the left, schematic input PSD corresponding to a Zernike radial order $n_{\text{rad}}=3$, with cut-off frequency $f_c = 1.5$ Hz (plain blue), residual PSD $S_{\text{res},2}$ at the output of the 2-stage CAO system with loop frequency $F_2 = 4$ kHz (dotted red) and residual PSD with a double integrator at $F_2 = 4$ kHz (black). On the right, from top to bottom: input PSD (light blue), PSD of residual signal $\bar{\phi}^{\text{res},1}$ at the output of 1st stage with loop frequency $F_1 = 1$ kHz (dashed magenta), inter-sampling signal ϕ^{is} PSD (thick green) and PSD of the residual inter-sampling signal after rejection by the 2nd stage RTF R_2 (dotted dark blue).

consider a similar noise variance for each stage, and a value of 410^{-4} [arb. units] has been chosen. This corresponds to a measurement noise variance about eight thousand times lower than that of the mode, that is a very high flux condition. We have tuned globally the two integrator gains of the CAO and also the gain and parameter of the double integrator and lead-lag filter to obtain the best residual variances: $6.0 \cdot 10^{-5}$ [arb. units] for the CAO, and $3.9 \cdot 10^{-5}$ [arb. units] for the double integrator. The corresponding rejection transfer functions and noise propagation transfer functions are shown in Fig. 6. On the right, the transfer function of the 1st stage noise rejected by the 2nd stage corresponds to the noise propagation transfer function of stage 1 multiplied by the stage 2 RTF (illustrated in dotted line on the left). It shows that the 1st stage gain cannot be set at a too high value because of the propagated measurement noise that attacks the 2nd stage RTF. Even in a very high flux situation, as can be seen in Fig. 9(a) for a magnitude of 3, the 1st stage gain must be chosen not too high to limit noise propagation.

The theoretical residual phases PSDs when noise is present noise are shown in Fig. 7. The

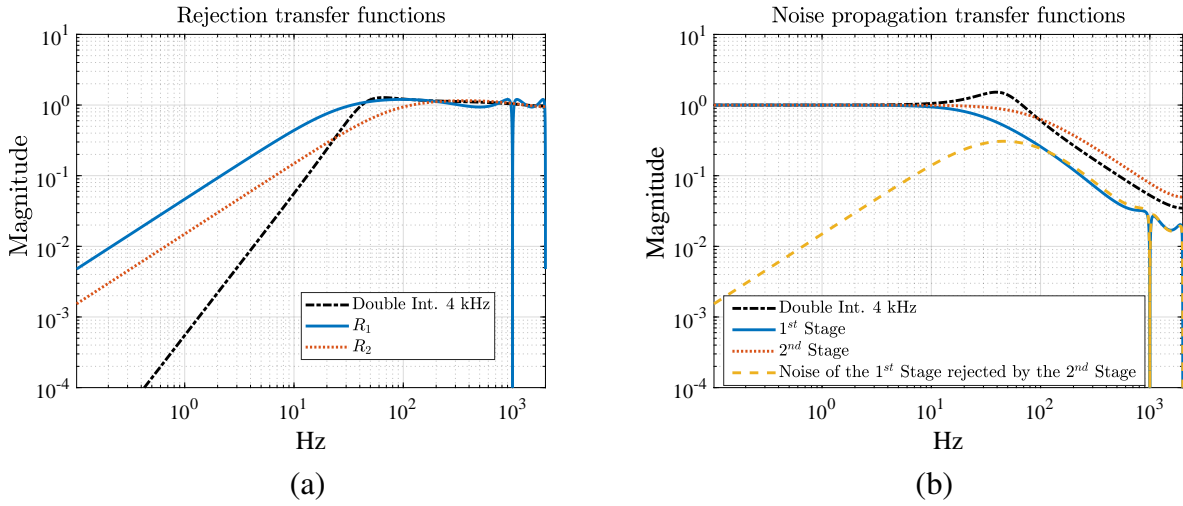


Fig 6 Transfer functions. On (a), RTFs with best tuning for each regulator: double integrator (Dashed black line), 1st stage (blue line), 2nd stage (dotted red line). On (b), noise propagation transfer functions: double integrator (dashed black line), 1st stage (blue line), 2nd stage (red dotted line), 1st stage noise propagation rejected by 2nd stage (yellow dashed line).

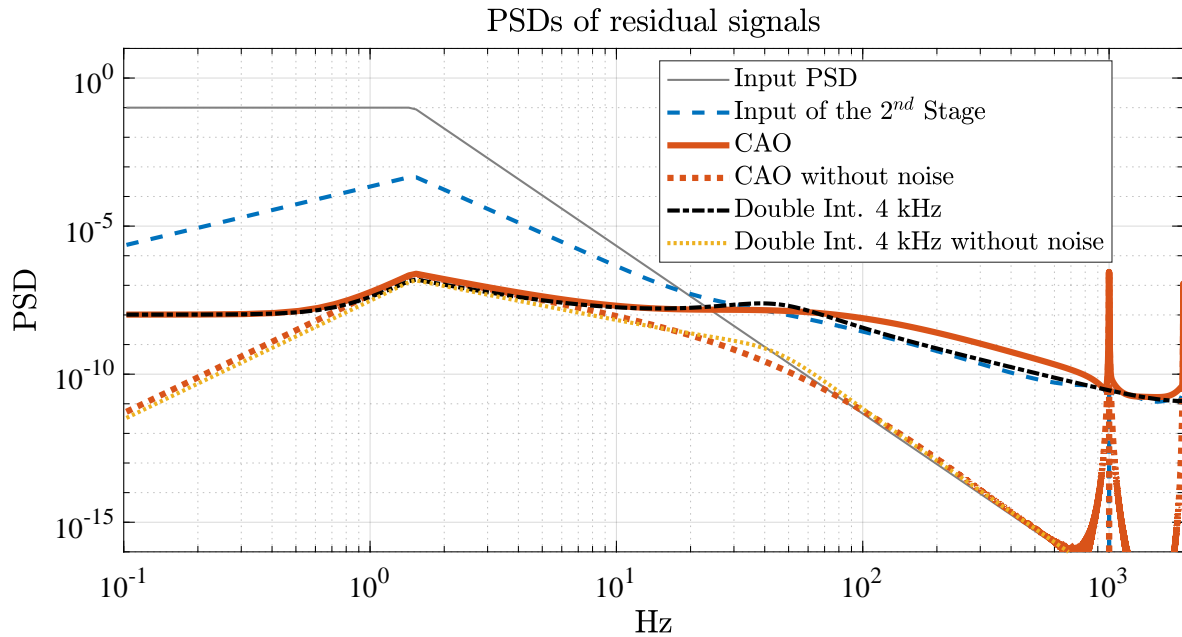


Fig 7 PSDs in presence of a measurement noise variance of $4 \cdot 10^{-4}$ [arb. units]: schematic modal input PSD (grey), input of the 2nd stage including inter-sampling signal (dotted blue), residual at the output of the CAO (plain red and dashed-dotted red for the case without noise), residual for the double integrator (dashed-dotted black and dotted yellow for the case without noise). The peaks of the 2nd stage input are at the same level than that of the CAO.

variance of the inter-sampling signal, $1.4 \cdot 10^{-5}$ [arb. unit], becomes now moderate compared with the total residual variance of $6.0 \cdot 10^{-5}$ [arb. units] for the CAO.

In summary, this two-stage CAO controller with loop frequencies $F_1 = 1$ kHz and $F_2 = 4$ kHz, when applied to standard atmospheric perturbations, will generate high frequencies (the inter-sampling signal due to the presence of the 1st stage) from low-frequency signals. The inter-sampling signal variance depends on the turbulence strength, with high frequencies not well attenuated by the 2nd stage because of the integrator overshoot. However, its impact is moderate in presence of measurement noise which propagation has a decisive impact on global performance. The low frequencies (until about twenty Hertz) will be on the other hand attenuated at the same level than that of a double integrator, and a better attenuation can be expected with the CAO at frequencies where the double integrator overshoots. We have also seen that the 1st stage propagated noise enters the 2nd stage as a disturbance, so that the value of the 1st stage integrator gain should be chosen not too high.

The CAO will provide a better contrast than the single stage system with good correction at low angular separations (corresponding to low order modes and low spatial frequencies¹⁰). It is clear here that a regulator designed specifically to compensate the 2nd stage input disturbance while limiting the 2nd stage noise propagation should further improve the global rejection, which is left for future work. The two-stage system presented here is simple to tune and its stability margins can be set separately in each loop by a proper choice of the two integrator gains. This modal control analysis has now to be completed by a performance analysis in terms of contrast and speckle lifetime, which is the purpose of the following section.

3 Performance Simulations

Operation and performance of a CAO system with two stages can be studied with the help of numerical simulations. As the CAO features two wavefront sensors, we have to make assumptions about the WFS types, the framerate at which these are running, and the beam-splitting between the two. We choose the Shack-Hartmann Sensor (SHS) to drive the 1st stage, consistent with the CAO concepts for SPHERE+¹⁵ and RISTRETTO¹⁶ which are currently in early development phases for ESO telescopes. The 2nd stages of these concepts (and our simulations) are driven by a unmodulated Pyramid WFS (PWS) which provides significantly better sensitivity and wavefront sensing accuracy than the SHS.⁴³ In particular, the advantage of a high-order AO system operated by a PWS is greatest near the image center which is where most Exoplanets appear and where the Exoplanet science case benefits most from a better WFS.^{10,46} The 1st stage's SHS is chosen to control about 800 Karhunen-Loève modes sampled by 36x36 subapertures at 1 kHz similar to what SPHERE SAXO⁴⁷ and the AOF provide.⁴⁸ The 2nd stage's PWS has a twice coarser one-dimensional sampling (18x18) and controls 200 modes, but runs four times faster (4 kHz) to efficiently reduce temporal error. These ballpark figures are consistent with what is considered for the 2nd stage AO systems under development mentioned above.

We explore two different options for the beam-splitting between the two stages: a) gray beam-splitting with a variable fraction of the I-band intensity distributed between the two stages, and b) dichroic beam-splitting with the 1st stage operating at a longer wavelength in the J-band, and the 2nd stage operating in I-band. These two beam-splitting cases are scientifically and technically motivated. The science case for SPHERE+ is focused on young stellar objects, and RISTRETTO is ultimately designed for the observations of Proxima b which is an approximately Earth-mass

planet orbiting our nearest neighboring star Proxima Centauri.⁴⁹ Temperate small planets were also found around several other very nearby stars,⁵⁰⁻⁵² and many more are expected to be identified by existing and future radial velocity (RV) instruments.^{53,54} The exoplanet host stars for these science cases, either very young or very nearby, are typically of a late spectral type and emit most of their flux in the I-band or longer wavelengths. This is also where important molecular lines can be found in the planetary spectra such as the A-band of molecular Oxygen at 760 nm which is the science wavelength we consider for our analysis. We choose the PWS of the 2nd stage to operate in I-band in order to have it as close as possible to the science wavelength and minimize chromatic residuals.¹⁰ The 1st stage WFS could then operate in the near IR, e.g., the J-band, and the light would be split between the two by a dichroic.

The 1st stage could also operate in I-band in which case a gray beam-splitter would be used. This would be a technically simple solution keeping the existing 1st stages of SPHERE and AOF, and we explore the best splitting ratio between the two stages hereafter. Table 1 summarizes the observation and instrument parameters used for the numerical simulations.

To simulate this CAO concepts, we use the AO simulation package OOMAO⁵⁵ running under MATLAB, and we implemented an integrated solution for simulating both stages in a single simulation run. For this, we generate the input phase at the fastest frequency (in our case, 4 kHz) and input an average of four consecutive turbulent phase screens to the 1st stage (1 kHz) at every fourth step and update the 1st stage DM. Then, the residual phase generated by the 1st stage is sent as an input to the 2nd stage at each step. This configuration allows us to take into account changes of the turbulent phase at the fast rate on the 2nd stage. We will now describe how the two main operation parameters of the CAO, the beam-splitting ratio between the two stages and their integrator gains, were optimized.

Table 1 System Parameters

Atmosphere	
r_0	0.10 [m] and 0.157 [m] at 550 [nm]
L_0	25[m]
Fractional r_0	[53.28 1.45 3.5 9.57 10.83 4.37 6.58 3.71 6.71]%
Altitude	[42 140 281 562 1125 2250 4500 9000 18000] m
Wind Speed	[15 13 13 9 9 15 25 40 21] m/s
Wind Direction	[38 34 54 42 57 48 -102 -83 -77] $\times\pi/180$
Telescope	
Diameter	8 [m]
Secondary Diameter	1.16 [m]
Photometric System	
I Band	Wavelength: $0.790e - 6$; Bandwidth: $0.150e - 6$
J Band	Wavelength: $1.215e - 6$; Bandwidth: $0.260e - 6$
Guide-Star (Proxima Centauri)	
I-J Color Index	2.06
Apparent magnitude (J)	5.35
Apparent magnitude (I)	7.41
Science Camera	
λ_i	I-band
1st Stage	
WFS	Shack-Hartmann
Order WFS	36×36
Control Modes	800
n_{pix} Camera	216×216 [pixels]
DM	37×37
λ_{wfs}	J-band or I-band
Transmission	0.2
QE	0.5
Readout Noise	0.5 [electron per pixel]
Loop Frequency F_1	1 kHz
2nd Stage	
WFS	Pyramid
Modulation	Unmodulated
Order WFS	18×18
Control Modes	200
n_{pix} Camera	216×216 [pixels]
DM	19×19
λ_{wfs}	I-band
Transmission	$0.2^{(a)}$
QE	0.5
Readout Noise	0.5 [electron per pixel]
Loop Frequency F_2	4 kHz

^(a)The additional transmission losses for the 2nd Stage due to the slightly increased number of optical surfaces is negligible and the same transmission has been assumed for both WFS.

3.1 Optimization of integrator gains and gray beam-splitting ratio

Depending on the WFS incident flux, the integrator gains must be adjusted for optimum performance. For simplicity, we assume a global gain for a given stage, but note that a modal gain optimization⁵⁶ can lead to an improved correction performance especially for faint stars. The incident flux on the WFS detector takes into account the assumed transmission to the detector listed in Table 1 and the WFS wavelength bandpass. For the dichroic beam-splitting, we assume a stellar with spectral type M5 (e.g. Proxima Centauri with I-J = 2.06) as a template red star, to calculate the flux intensities in the different bands. For example, a J = 0.94 and I = 3 star provides 15710 and 2600 photons/subaperture/frame on stage 1 and 2, respectively. For the gray beam-splitting case, five different split ratios between the 1st stage and the 2nd stage were simulated: 20%/80%, 35%/65%, 50%/50%, 65%/35% and 80%/20%. For example, an I = 3 star observed with an 80/20 beam-splitter provides 2199 and 521 photons/subaperture/frame on stage 1 and 2, respectively. Here, the relative photon flux approximately corresponds to the split ratio, because the 2nd stage has four times bigger subapertures than the 1st stage but runs four times faster.

In order to determine the optimum gray beam-splitting ratio, we first individually optimize the integrator gains for both stages depending of the incident flux and split ratio. These results are shown in Fig. 8. Apart from the faintest stars, the best overall performance is obtained when 80% of the light is sent to the 1st stage and 20% is sent to the 2nd stage for both values of r_0 evaluated. This reflects the higher sensitivity of the PWS when compared with the SHS. The 2nd stage maintains a high performance on significantly lower photon flux than what is required for the 1st stage.

Then we jointly optimize the gain values of both stages for both beam-splitting cases. In order

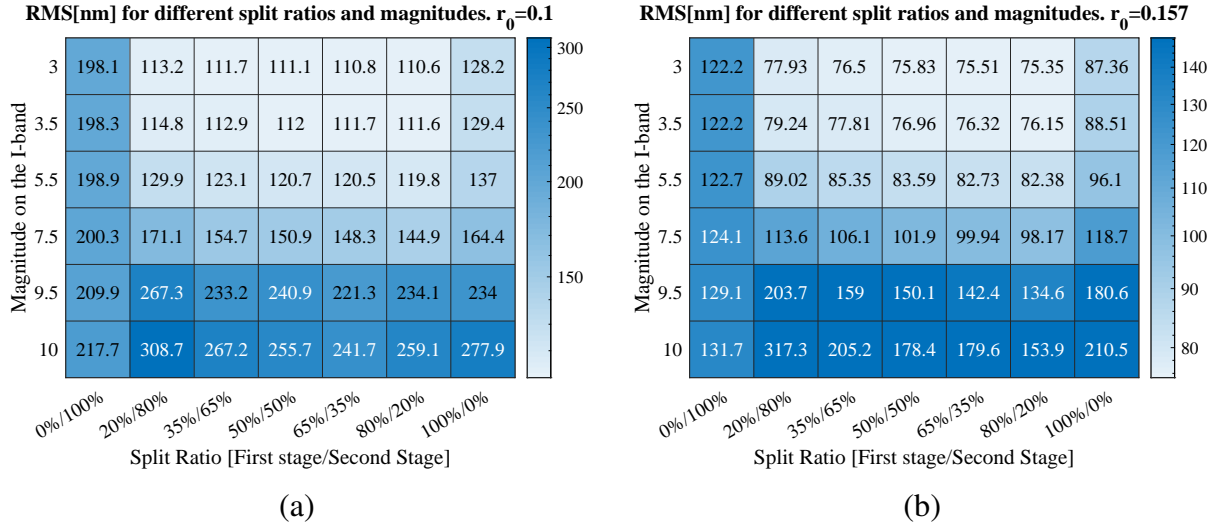


Fig 8 Wavefront error [nm] for different split-ratios (gray beam-splitter case) and magnitude. On the left side, the simulation were done using $r_0 = 0.1$ [m] and on the right side $r_0 = 0.157$ [m]. The darker the color, the bigger the WFE. In terms of RMS, the best overall performance is achieved using an 80%/20% split ratio for magnitudes up to 8 in I-band.

to limit the size of the already large simulation parameter grid, we only consider the 80/20 split ratio for this analysis. The rationale for the joint optimization of the gains is that the PSD of the input disturbance to the 2nd stage is modified by the rejection transfer function (RTF) of the 1st stage controller (as described in Sec. 2.2). A higher gain for the 1st stage will lead to better low frequency rejection but more overshoot at high frequencies. It therefore shuffles energy from low to high frequencies where the correction by the 2nd stage is less effective. Hence, a 1st stage gain that optimizes its own residual wavefront variance may not lead to the minimum residual wavefront variance at the output of the 2nd stage. Figure 9 shows an example results of the joint gain optimization for a bright, a medium and a faint guide star, respectively. For each magnitude we diminish the 1st stage closed-loop gain obtained by the individual optimization from a factor 1 to 0.5 in 10% steps and we amplify the 2nd stage closed-loop gain obtained by the individual optimization from a factor 1 to 1.5 in 10% steps. The resulting gains for stage 1 and 2 are shown

on the Y- and X-axes of the heatmaps, respectively. The results for the individual optimization of the integrator gains are shown in red, while the joint optimization results are shown in green. We see that in general, the joint gain optimization leads to a reduced 1st stage gain with respect to the individual optimization but maintains the 2nd stage gain. For bright magnitude = 3 stars, there is no evident improvement in performance by using the joint gain optimization probably because the high-frequency amplification mostly consists of noise, so the reduction of the fitting error of modes not controlled by the second stage is more relevant than the amplification of the low level of noise at high temporal frequencies.

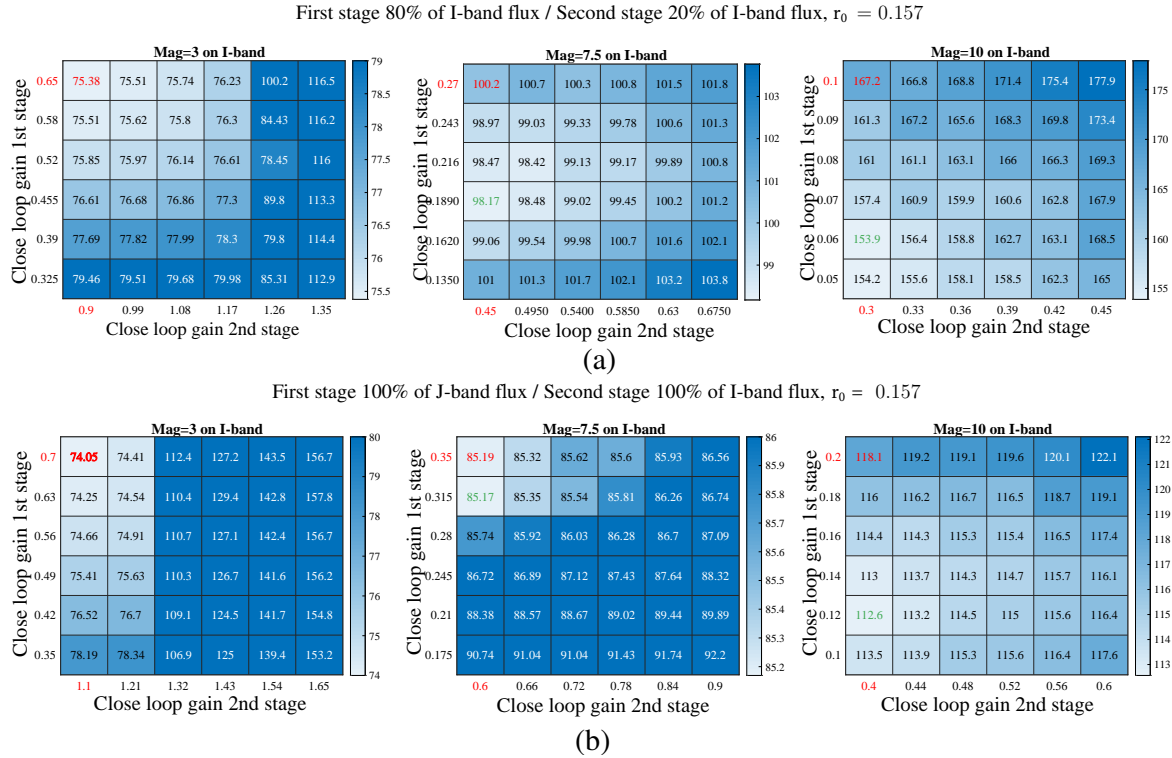


Fig 9 Residual WFE [nm RMS] as a function of close loop gain and three different magnitudes. Panel a) on the top shows the gray beam-splitting case using a 80%/20% split-ratio, while on panel b) on the bottom, we assume a dichroic beam-splitter. The starting point of the joint optimization are the individually optimized gains shown in red with the corresponding WFE in the upper left corner. From there, we explored reduced stage 1 gains and increased stage 2 gains. The minimum residual WFE obtained by the joint optimization is shown in green. For the bright guide star case ($I=3$), the individually optimized gains were already optimum.

Note that the optimum gains for the 2nd stage include the optical gains of the PWS^{57,58} which

are always smaller than one. Using a published method⁵⁸ we calculate optical gain values ranging between 0.75 for $r_0 = 0.1\text{m}$ and 0.87 for $r_0 = 0.157\text{m}$ as shown in Fig. 10. The optical gains are relatively large because the 2nd stage PWS only sees the residuals of the 1st stage and therefore operates in a very small residual WFE regime. Then, the pure integrator control gain would be obtained by multiplying the 2nd stage gain with the respective optical gain.

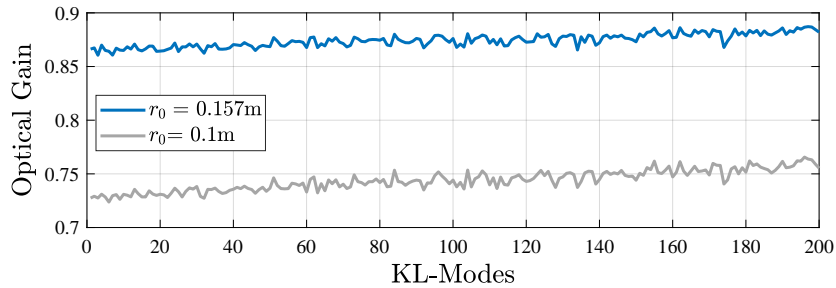


Fig 10 Optical gains for the 2nd stage PWFS as a function of the Karhunen-Loève modes for two different values of the Fried parameter r_0 .

3.2 Residual WFE and contrast performance

Having determined the optimum integrator gains and split ratios for the CAO system, we can now compare the performance of both splitting concepts and quantify the correction improvement provided by the 2nd stage. For the gray beam-splitting case, 80% of the flux is sent to the 1st stage and 20% is sent to the 2nd stage. This ratio is optimum for all but the faintest stars as shown in Sec. 3.1, and it is kept fixed because a single optical beam-splitters would not allow one to change the ratio depending on observing conditions. For the dichroic beam-splitting case, the star is assumed to have a red I-J color of 2.06, as motivated in Sec. 3.1.

Figure 11 shows the CAO systems' residual WFE after 10,000 iterations on the 1st stage (i.e., after 10 seconds of closed-loop operation) as a function of guide star I-band magnitude for good and median seeing values. Figure 11 shows that the CAO (orange dashed line) consistently outper-

forms the single stage AO for all guide star magnitudes independently from how the beam-splitting is done. Not surprisingly, dichroic beam-splitting leads to a better correction performance overall because it provides more photons for each WFS individually, leading to a better correction performance overall. The curves exhibit the expected behavior of a rather constant bright guide star performance dominated by fitting error residuals and a degradation for fainter stars where measurement noise is dominating the error budget.

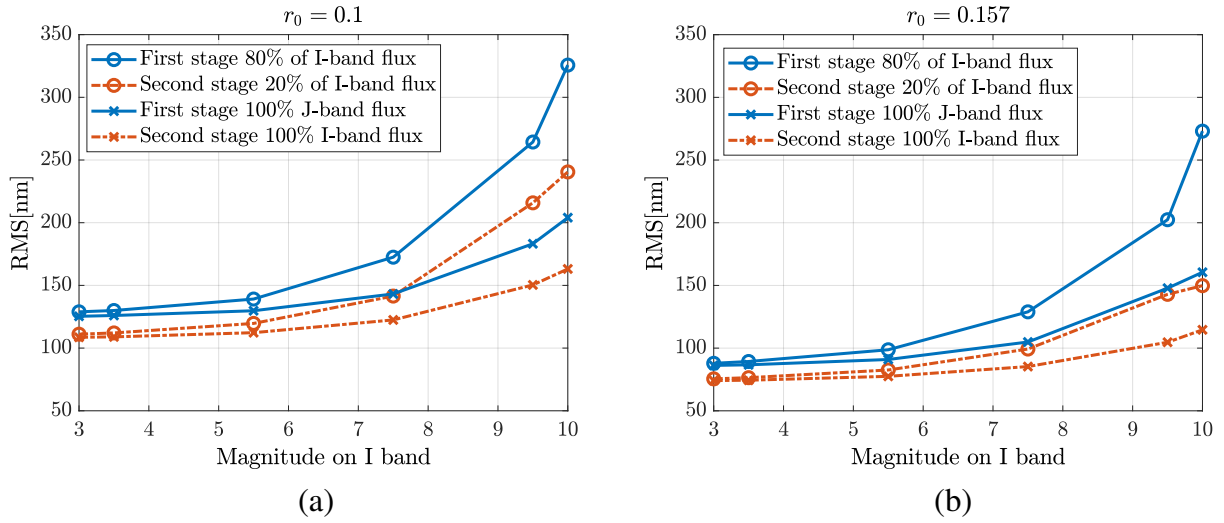


Fig 11 RMS in nanometers in terms of magnitude for the 1st stage only (solid blue line) and with the 2nd stage (dashed orange line) for (a) $r_0 = 0.1$ and (b) $r_0 = 0.157$. In the case where both wavefront sensors work on the I-band, the full flux is divided in a 80%/20% split ratio between both stages (circle markers). In the other case, the flux is divided in different wavelengths for each stage, and 100% of the flux is sent (cross markers).

Besides the residual RMS WFE, the residual point spread function (PSF) contrast presents another important performance metric for high-contrast imaging. We calculate the residual PSF from the residual WFE assuming that Airy diffraction pattern has been removed by an idealized perfect coronagraph.⁵⁹ The one-dimensional residual PSF contrast is then given by the standard deviation of the flux intensities in a thin annulus of a given angular radius normalized by the peak intensity of the non-coronagraphic PSF.

Figure 12 shows the residual coronagraphic PSF and its contrast for the gray beam-splitting

case in median and good seeing, and Fig. 13 shows the same for the dichroic beam-splitting case. The simulated observations represent the flux case of Proxima Centauri with $I = 7.4$, so neither very bright nor very faint. Imaging is done in I-band where the A-band of molecular oxygen is located. The improvement provided by the fast second correction stage is demonstrated by the better contrast in the controlled region of the 2nd stage DM at separations smaller than about $9 \lambda/D$. The 2nd stage removes the elongated wind-driven halo⁶⁰ which is a signpost for the temporal error of the AO and improves the residual halo contrast at these angular separations by almost one order of magnitude. This is consistent with the analytical prediction that the temporal error is proportional to $f_c^{-5/3}$ (with f_c denoting the correction frequency), so one would expect an about ten times improvement for a four times faster correction.

The best performance for the Proxima Centauri case is achieved by beam-splitting with a dichroic and reaches a contrast of 2×10^{-4} for good seeing at the maximum angular separations of Proxima b of about 40 mas or $2 \lambda/D$ for an 8-m telescope observing at 760 nm. Such a contrast performance should allow us to detect Oxygen in a hypothetical Proxima b atmosphere with an Earth-like composition in a few hundred hours.⁶¹ Such an observation would require the AO WFS to work at a waveband slightly longer than I-band (e.g. between 800nm and 950nm) to send all the 760 nm photons to the spectrograph..

Using a PWS for the fast second stage combines several beneficial effects at the same time. It reduces temporal error, aliasing error⁶² and noise error.¹⁰ The aliasing error of the 1st stage SHS⁶³ should be around 30nm and 45nm RMS for an r_0 of 0.157m and 0.1m, respectively, while the temporal errors⁶⁴ for an assumed time delay of 2 frames, so 2ms, should be 50nm and 75nm. The photon-noise limited SHS centroiding error⁶⁵ assuming a noise propagation on n reconstructed modes proportional to $\log(n)$ ⁶³ yields about 50nm RMS. Therefore, aliasing and photon noise

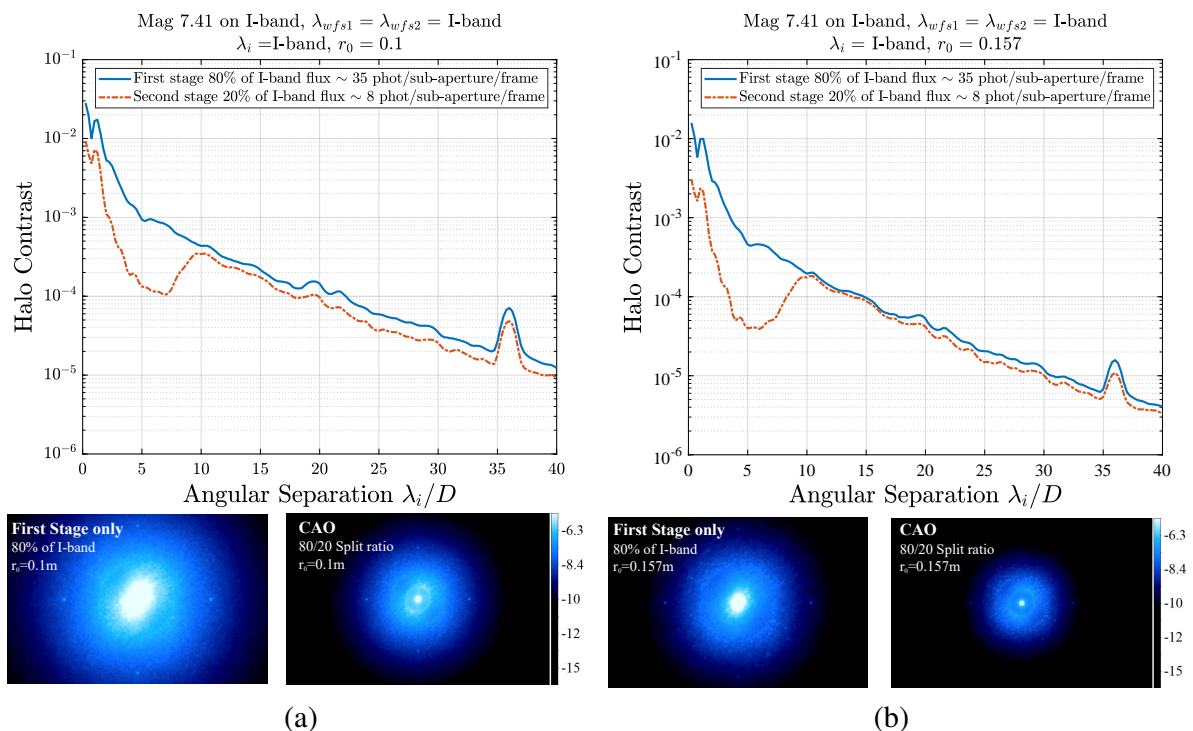


Fig 12 Contrast performance and PSF for $r_0 = 0.1$ (a) and $r_0 = 0.157$ (b). Both stages operate their WFS in I-band, and the optimum gray beamsplitting ratio (80%/20%) was used. Scientific analysis is done in I-band as well.

cannot be neglected and a significant contrast improvement is already expected when adding a slow 2nd stage with a PWS.

The yellow dotted line on Figure. 13 shows the simulated contrast from a “slow” 1kHz 2nd stage PWS. The reduction of aliasing and the higher sensitivity of the PWS compared to the SHS already results in a significant gain in contrast of a factor 2-3. Another factor 3-5 is then gained by running the second stage faster and reduce the temporal error as seen by the red dotted line on the same figure.

Figure. 14 shows how the contrast at 40 mas is improved by the 2nd stage as a function of stellar I-band magnitude. Again, the CAO system provides a contrast improvement of roughly one order of magnitude when compared to the single stage AO. Similar to the residual wavefront error shown in Fig. 11, we see that the correction and contrast performance degrade with stellar magnitude due

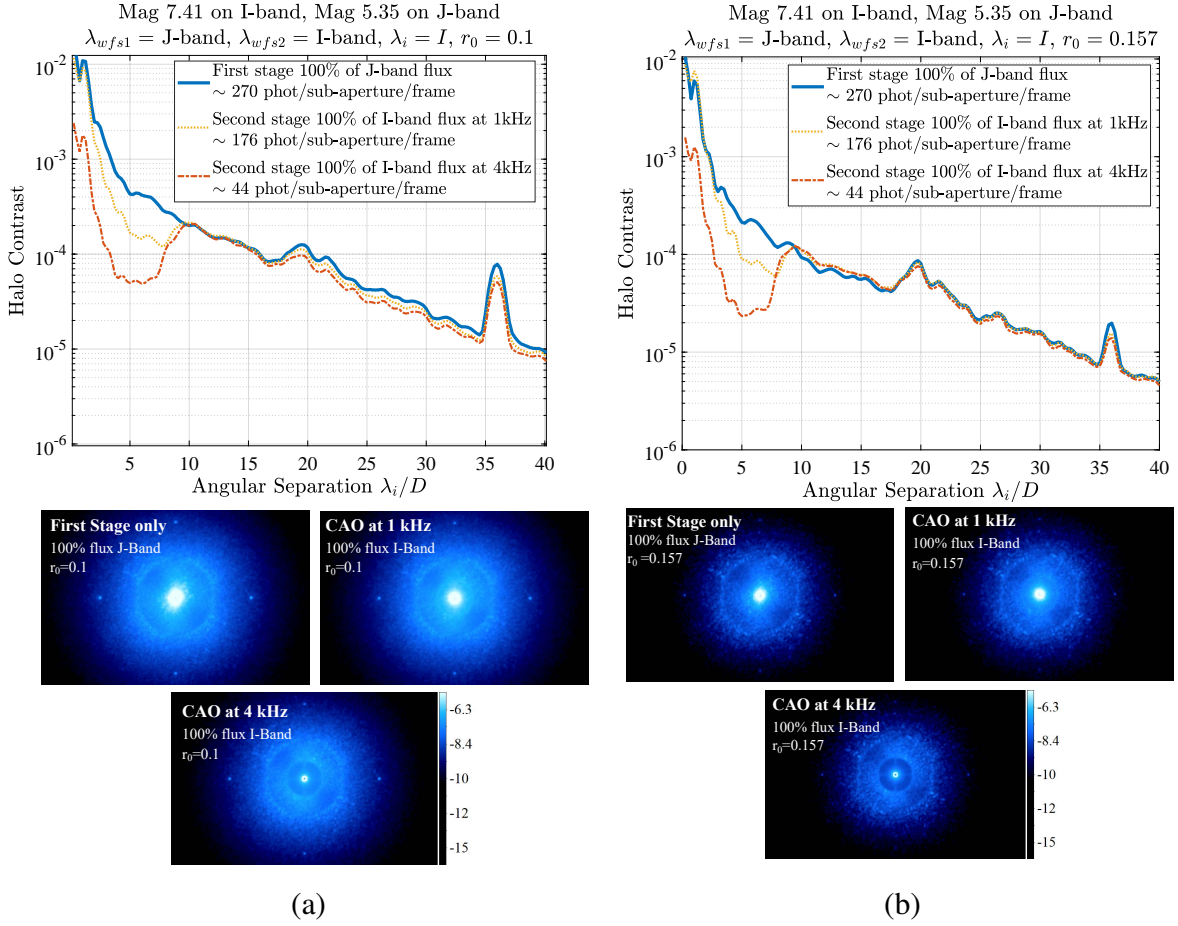


Fig 13 Contrast performance and PSF for $r_0 = 0.1$ (a) and $r_0 = 0.157$ (b) and dichroic beamsplitting. All the J-Band flux was sent to the 1st stage, and all the I-band flux was sent to the 2nd stage. Scientific analysis is done in I-band.

to the increased noise and reduced optimum integrator gains. In contrast to the residual wavefront error, the contrast in the bright end does not level out because of a dominating fitting error which occurs at spatial frequencies beyond the correction radius of the AO and would not affect the contrast at small angular separations. We rather see that aliasing and residual temporal error for the system approaching the maximum stable gain and thereby operating at its maximum correction bandwidth set the contrast cap for very bright stars. In the faint end, the CAO system degrades less rapidly because its 2nd stage stage is operated by the more sensitive Pyramid WFS.

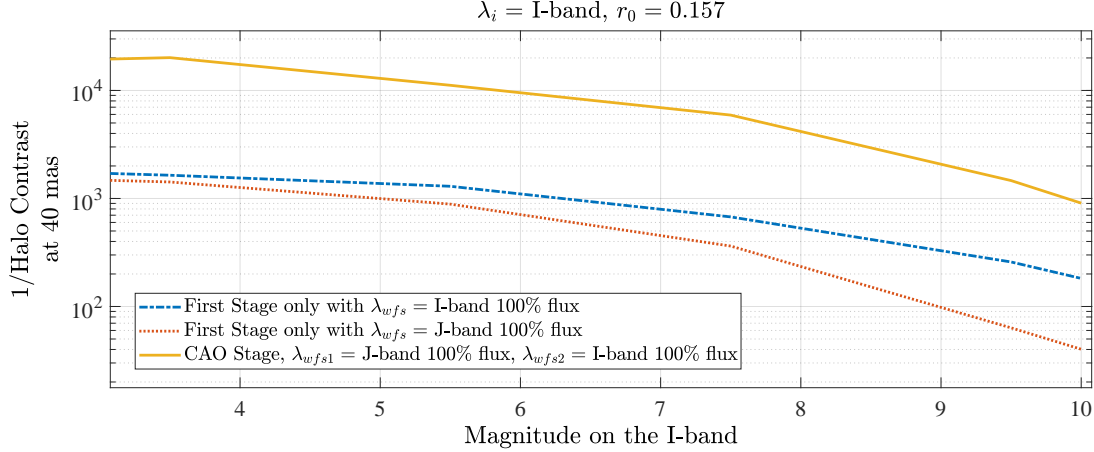


Fig 14 PSF residual contrast as a function of magnitude at an angular separations of 40 mas.

3.3 Analysis of AO residual speckle lifetime

Another important parameter for HCI is the lifetime of speckles in the AO residual PSF. If we assume that the speckle noise would reduce with $1/\sqrt{t_{dc}}$, where t_{dc} is the speckle decorrelation time, a residual speckle halo with typical intensity contrast of about 10^{-5} would require 10^6 independent realizations to reach a level of 10^{-8} in the absence of other speckle correction techniques such as angular, spectral or polarimetric differential imaging. Depending on the speckle lifetime, accumulating that many realizations of the speckle pattern can be a very long process.

Long-lived quasi-static speckles are produced by instrument aberrations, which are left uncorrected by the AO system⁶⁶ and are one of the dominating factors affecting contrast especially at low angular separations.¹⁰ These residual aberrations can occur in the instrument's science camera optical path, which is not seen by the AO WFS, or in the optical path to the AO WFS, which is not seen by the science camera. Therefore they are called non-common path aberrations (NCPA). NCPA change only slowly on timescales on which the instrument orientation and the gravity vector changes during an observation tracking a target in the sky. Also, temperature variations that produce thermal expansions in the instrument may introduce NCPA. Residuals from the atmo-

spheric turbulence can induce a fast partial decorrelation of the PSF over a few seconds before transiting to a linear decorrelation regime at small angular separations.⁶⁷ A refined analysis further revealed another speckle decorrelation time scale of less than 2 ms which can be attributed to the AO correction.⁶⁸

Our simulations do not include NCPA, so we are solely looking at the temporal evolution of residual atmospheric turbulence speckle intensities. Assuming Taylor’s frozen flow hypothesis, it was shown in Ref. 69 that an integrator-controlled AO system does not change the speckle lifetime compared to uncorrected turbulence but leads to an overall reduction in speckle intensity. This is explained by the idea that the correction always trails behind incoming turbulence leaving a residual with unchanged temporal characteristics. Moreover, the speckle lifetime is proportional to the ratio between telescope diameter (D) and wind-speed (v), more specifically $0.6D/v$. In the case of the VLT, with winds of 10 m/s, the atmospheric residual speckle lifetime is therefore of the order of half a second, while speckles are expected to decorrelate on timescales of several seconds in the ELT case. Such lifetimes would lead to unfeasible long exposure time requirements (more than 100 hours for the 10^6 independent realizations motivated above) for reaching very high contrast. These considerations underline the high interest in reducing the lifetime of residual atmospheric speckles, even if the frozen flow assumption may be pessimistic in this context.

In Sec. 2.2, we showed that the low frequency part of the CAO’s loop correction transfer function is very similar to the one of a double-integrator controller. The CAO system therefore presents a much more efficient reduction of the aberration energy at low temporal frequencies, and an effect on the speckle lifetime should be observable in the image plane. Therefore, we apply published analysis⁷⁰ on our simulated coronagraphic images and compare speckle lifetimes for single and double stage AO correction. We analysed three annular regions at different angular separations

from the PSF center: $A_1 = 2-5[\frac{\lambda}{D}]$, $A_2 = 5-8[\frac{\lambda}{D}]$ and $A_3 = 12-15[\frac{\lambda}{D}]$ as indicated in Fig. 15. While A_1 and A_2 are inside the correction radius and controlled by both stages of the CAO, A_3 is only affected by the 1st stage and could therefore show a different speckle lifetime. We simulated a short 2.5 seconds observation with $r_0 = 0.157\text{m}$ and an elevated wind speed, 50% higher than the wind speed used for the performance simulations (See Table 1). For each of the three regions, we arranged the 2.5 seconds worth of imaging data in a matrix which contains the evolution over time for each pixel. We then subtracted the mean intensity of each pixel and calculated the temporal autocorrelation functions. Finally, the autocorrelation functions of all the pixels were averaged to derive the typical temporal correlation of the residual speckles in the three considered regions.

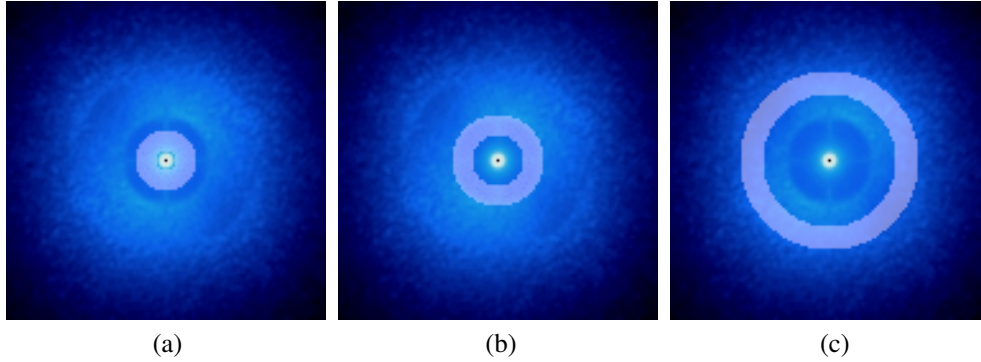


Fig 15 Long exposure perfect coronagraph PSF with different regions A over imposed. (a): $A_1 = 2-5[\frac{\lambda}{D}]$ (b): $A_2 = 5-8[\frac{\lambda}{D}]$ and (c): $A_3 = 12-15[\frac{\lambda}{D}]$.

The results are shown Fig. 16. In the regions A_1 and A_2 we clearly see the effect of the 2nd stage. While the lifetime of residual speckles after the 1st stage is of the order of 0.15 seconds, it is reduced to just a few ms after the 2nd stage. This reduction of a factor 30-50 is much larger than the fourfold increased correction speed offered by the 2nd stage. We also see that the decorrelation time in region A_3 is not affected by the CAO. This is the expected behavior because A_3 is outside of the control region of the 2nd stage. Compared to the relatively long lifetime of residual atmospheric

speckle of a single stage AO, the fast decorrelation of residual speckles of the CAO will help to smoothen the residual PSF efficiently. The more than 100 hours for 10^6 independent realizations would then shorten to just a few hours, which is consistent with typical HCI observing times.

$$r_0 = 0.157 \lambda_{WFS1} = \text{J-band } \lambda_{WFS2} = \text{I-band } \lambda_i = \text{I-band}$$

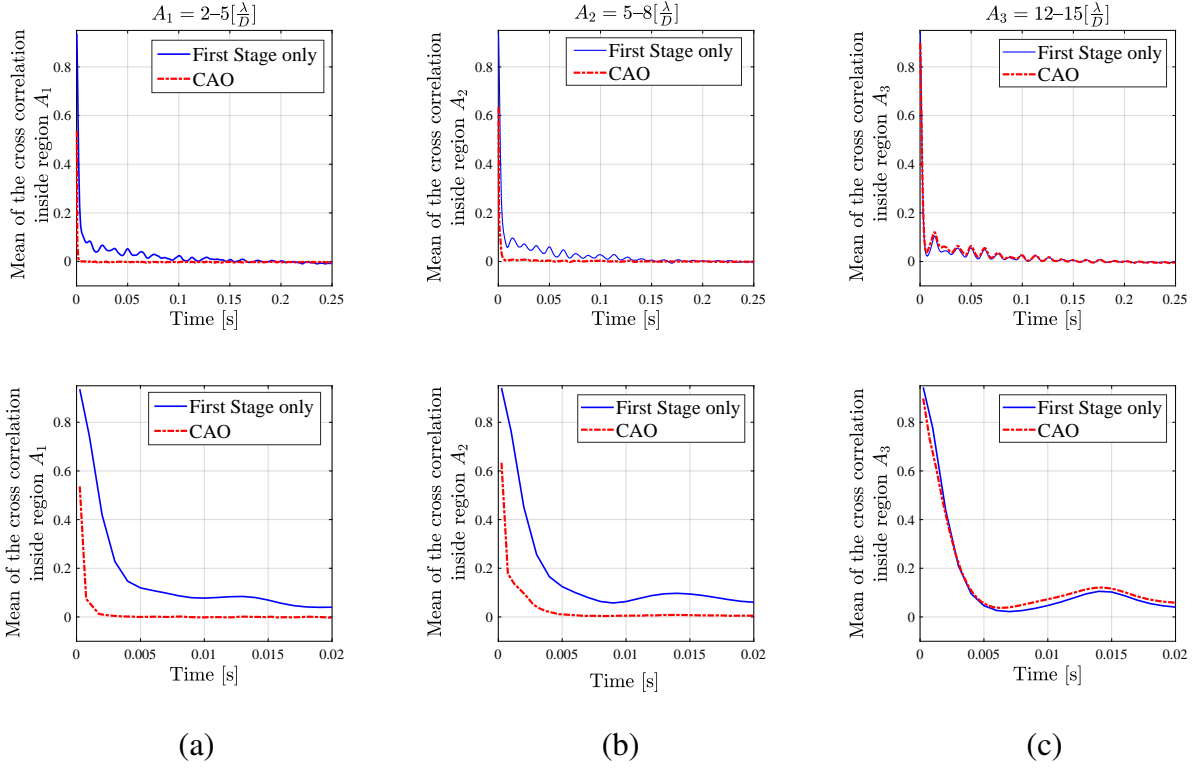


Fig 16 Temporal decorrelations of all the pixels inside A for three different regions: (a) $A_1 = 2-5[\frac{\lambda}{D}]$, (b) $A_2 = 5-8[\frac{\lambda}{D}]$ and (c) $A_3 = 12-15[\frac{\lambda}{D}]$. The panels on the bottom zoom in on very short timescales.

4 Summary and discussion

A two-stage CAO system with a faster 2nd stage presents an efficient way to significantly improve the contrast performance of an existing XAO system limited by temporal error which is of paramount interest for the Exoplanet science case. While a single stage XAO system running at high speed and equipped with a high order DM could probably provide better results than the proposed CAO system, it would require a more powerful RTC and a fast response and large stroke

of the high-order DM. The proposed CAO system instead provides a cost and resource effective solution to improve the performance of an existing XAO system. Further benefits are that the 2nd stage can easily be integrated and tested stand-alone and retrofitted into an existing instrument. The main complication introduced by this concept is that the 1st stage increases the relative content of high temporal frequency disturbance input to the 2nd stage because of its controller overshoot and the inter-sampling signal (see Sec.2.2). Possibilities to mitigate this effect include running the 1st stage at a reduced gain in noisy conditions, or designing the 2nd stage controller in a way that effectively copes with the inter-sampling signal. A straightforward solution would be to include a notch filter in the 2nd stage loop. Also, a global design of an optimized 2nd stage predictive controller would be of great interest. These developments deserve a complete study and are left for future work. We also showed that the low temporal frequency rejection of the CAO is partly the same than that of a SCAO system controlled with a double-integrator and is much higher than that of a SCAO system controlled with a standard integrator.

Numerical simulations of a 1st stage SHS AO system running at 1 kHz (similar to the existing VLT-SPHERE or AOF) show that a fast 2nd stage employing a sensitive WFS such as the unmodulated PWS would improve the correction performance for all GS magnitudes. A simple integrator control for both stages where the 2nd stage runs at four times the framerate of the first one increases the contrast by about one order of magnitude which would translate into a similar reduction of science exposure time required to reach a certain S/N. The integrator gains of both stages must be jointly optimized to reach optimum performance to cope with the 1st stage altering the input disturbance to the 2nd stage. The two stage CAO can provide at $2 \lambda/D$ an I-band contrast of the order 1:5000 for an 8-m telescope with a 1st stage AO correcting 800 modes at a framerate of 1 kHz. Such a performance would for example bring the detection of oxygen in the atmosphere

of Proxima b (if it were present at an Earth-like abundance) within reach.

AO systems which already use the sensitive PWS and run at high framerates such as KPIC⁷¹ or MagAO-X⁷² are already able to reduce all relevant AO residual error terms (aliasing, temporal, and noise errors) to the minimum and therefore wouldn't benefit from a CAO architecture in the same way as the system we have studied. In particular, the double-integrator behavior of the CAO for low frequencies can also be obtained by a single-stage AO.

Finally, a CAO with a four times faster 2nd stage reduces the decorrelation or lifetime of atmospheric turbulence speckles by a factor 30-50 over the lifetime observed with the 1st stage only. While this obviously does not reduce photon noise, it helps to smoothen the residual halo more rapidly and reduce its "granularity". This CAO therefore leads to a reduction of atmospheric speckle noise such that spatial low-pass filtering methods can be used to improve the final image contrast effectively.

Acknowledgments

This work has received funding from the European Unions Horizon 2020 research and innovation program, grant agreement No 730890.

References

- 1 M. Mayor and D. Queloz, "A Jupiter-mass companion to a solar-type star," *Nature* **378**, 355–359 (1995).
- 2 C. Marois, B. Macintosh, T. Barman, *et al.*, "Direct Imaging of Multiple Planets Orbiting the Star HR 8799," *Science* **322**, 1348 (2008).
- 3 C. Marois, B. Zuckerman, Q. M. Konopacky, *et al.*, "Images of a fourth planet orbiting HR 8799," *Nature* **468**, 1080–1083 (2010).

- 4 A.-M. Lagrange, M. Bonnefoy, G. Chauvin, *et al.*, “A Giant Planet Imaged in the Disk of the Young Star beta Pictoris,” *Science* **329**, 57 (2010).
- 5 J. Rameau, G. Chauvin, A.-M. Lagrange, *et al.*, “Discovery of a Probable 4-5 Jupiter-mass Exoplanet to HD 95086 by Direct Imaging,” *ApJl* **772**, L15 (2013).
- 6 V. Bailey, T. Meshkat, M. Reiter, *et al.*, “HD 106906 b: A Planetary-mass Companion Outside a Massive Debris Disk,” *ApJl* **780**, L4 (2014).
- 7 B. Macintosh, J. R. Graham, T. Barman, *et al.*, “Discovery and spectroscopy of the young jovian planet 51 Eri b with the Gemini Planet Imager,” *Science* **350**, 64–67 (2015).
- 8 G. Chauvin, S. Desidera, A.-M. Lagrange, *et al.*, “Discovery of a warm, dusty giant planet around HIP 65426,” *A&A* **605**, L9 (2017). Publisher: EDP Sciences.
- 9 G. P. P. L. Otten, A. Vigan, E. Muslimov, *et al.*, “Direct characterization of young giant exoplanets at high spectral resolution by coupling SPHERE and CRIRES+,” *A&A* **646**, A150 (2021). eprint: 2009.01841.
- 10 O. Guyon, “Limits of Adaptive Optics for High-Contrast Imaging,” *ApJ* **629**, 592–614 (2005).
- 11 J. Chilcote, Q. Konopacky, R. J. D. Rosa, *et al.*, “GPI 2.0: upgrading the Gemini Planet Imager,” in *Ground-based and Airborne Instrumentation for Astronomy VIII*, C. J. Evans, J. J. Bryant, and K. Motohara, Eds., **11447**, 394 – 407, SPIE (2020).
- 12 J. R. Males and O. Guyon, “Ground-based adaptive optics coronagraphic performance under closed-loop predictive control,” *Journal of Astronomical Telescopes, Instruments, and Systems* **4**, 019001 (2018).
- 13 C. Z. Bond, S. Cetre, S. Lilley, *et al.*, “Adaptive optics with an infrared pyramid wavefront sensor at Keck,” *JATIS* **6**(3), 1 – 21 (2020).

- 14 J. Lozi, O. Guyon, N. Jovanovic, *et al.*, “SCEXAO, an instrument with a dual purpose: perform cutting-edge science and develop new technologies,” in *Adaptive Optics Systems VI*, L. M. Close, L. Schreiber, and D. Schmidt, Eds., *Society of Photo-Optical Instrumentation Engineers (SPIE) Conference Series* **10703**, 1070359 (2018). [eprint: 1809.08301](#).
- 15 A. Boccaletti, G. Chauvin, D. Mouillet, *et al.*, “SPHERE+: Imaging young Jupiters down to the snowline.” [arXiv: Earth and Planetary Astrophysics](#) (2020).
- 16 B. Chazelas, C. Lovis, N. Blind, *et al.*, “RISTRETTO: a pathfinder instrument for exoplanet atmosphere characterization,” in *Adaptive Optics Systems VII*, **11448**, 1144875, International Society for Optics and Photonics (2020).
- 17 M. D. Perrin, A. Sivaramakrishnan, R. B. Makidon, *et al.*, “The Structure of High Strehl Ratio Point-Spread Functions,” *ApJ* **596**, 702–712 (2003).
- 18 J. L. Beuzit, A. Vigan, D. Mouillet, *et al.*, “SPHERE: the exoplanet imager for the Very Large Telescope,” *A&A* **631**, A155 (2019). [eprint: 1902.04080](#).
- 19 P. Y. Madec, R. Arsenault, H. Kuntschner, *et al.*, “Adaptive Optics Facility: from an amazing present to a brilliant future...,” in *Adaptive Optics Systems VI*, L. M. Close, L. Schreiber, and D. Schmidt, Eds., *Society of Photo-Optical Instrumentation Engineers (SPIE) Conference Series* **10703**, 1070302 (2018).
- 20 C. Dessenne, P.-Y. Madec, and G. Rousset, “Modal prediction for closed-loop adaptive optics,” *Optics Letters* **22**, 1535–1537 (1997).
- 21 D. T. Gavel and D. Wiberg, “Toward Strehl-optimizing adaptive optics controllers,” in *Adaptive Optical System Technologies II*, P. L. Wizinowich and D. Bonaccini, Eds., *Society of Photo-Optical Instrumentation Engineers (SPIE) Conference Series* **4839**, 890–901 (2003).

- 22 B. Le Roux, J.-M. Conan, C. Kulcsár, *et al.*, “Optimal control law for classical and multiconjugate adaptive optics,” *Journal of the Optical Society of America A* **21**, 1261 (2004).
- 23 L. A. Poyneer, B. A. Macintosh, and J.-P. Véran, “Fourier transform wavefront control with adaptive prediction of the atmosphere,” *Journal of the Optical Society of America A* **24**, 2645 (2007).
- 24 P. Piatrou and M. C. Roggemann, “Performance study of Kalman filter controller for multiconjugate adaptive optics,” *Applied optics* **46**(9), 1446–1455 (2007). Publisher: Optical Society of America.
- 25 K. Hinnen, M. Verhaegen, and N. Doelman, “Exploiting the spatiotemporal correlation in adaptive optics using data-driven H_2 -optimal control,” *JOSA A* **24**(6), 1714–1725 (2007). Publisher: Optical Society of America.
- 26 C. Petit, J.-M. Conan, C. Kulcsár, *et al.*, “Linear quadratic Gaussian control for adaptive optics and multiconjugate adaptive optics: experimental and numerical analysis,” *J. Opt. Soc. Am. A* **26**, 1307–1325 (2009). Publisher: OSA.
- 27 R. Fraanje, J. Rice, M. Verhaegen, *et al.*, “Fast reconstruction and prediction of frozen flow turbulence based on structured Kalman filtering,” *JOSA A* **27**, A235–A245 (2010). Publisher: OSA.
- 28 C. Kulcsár, H.-F. Raynaud, C. Petit, *et al.*, “Minimum variance prediction and control for adaptive optics,” *Automatica* **48**, 1939–1954 (2012).
- 29 C. M. Correia, K. Jackson, J.-P. Véran, *et al.*, “Spatio-angular minimum-variance tomographic controller for multi-object adaptive-optics systems,” *Appl. Opt.* **54**, 5281 (2015).

- 30 O. Guyon and J. Males, “Adaptive optics predictive control with empirical orthogonal functions (eofs).” arXiv: Instrumentation and Methods for Astrophysics (2017).
- 31 M. Glück, J. Pott, and O. Sawodny, “Model Predictive Control of Multi-Mirror Adaptive Optics Systems,” in *2018 IEEE Conference on Control Technology and Applications (CCTA)*, 909–914 (2018).
- 32 L. Prengère, C. Kulcsár, and H.-F. Raynaud, “Zonal-based high-performance control in adaptive optics systems with application to astronomy and satellite tracking,” *JOSA A* **37**(7), 1083–1099 (2020). Publisher: Optical Society of America.
- 33 X. Liu, T. Morris, C. Saunter, *et al.*, “Wavefront prediction using artificial neural networks for open-loop adaptive optics,” *Monthly Notices of the Royal Astronomical Society* **496**, 456–464 (2020).
- 34 C. Dessenne, P.-Y. Madec, and G. Rousset, “Sky implementation of modal predictive control in adaptive optics,” *Optics letters* **24**(5), 339–341 (1999). Publisher: Optical Society of America.
- 35 N. Doelman, R. Fraanje, and R. den Breeje, “Real-sky adaptive optics experiments on optimal control of tip-tilt modes,” in *Second International Conference on Adaptive Optics for Extremely Large Telescopes.*, 51 (2011).
- 36 G. Sivo, C. Kulcsár, J.-M. Conan, *et al.*, “First on-sky SCAO validation of full LQG control with vibration mitigation on the CANARY pathfinder,” *Optics express* **22**(19), 23565–23591 (2014). Publisher: Optical Society of America.
- 37 O. Lardière, D. Andersen, C. Blain, *et al.*, “Multi-object adaptive optics on-sky results with

- Raven,” in *Adaptive Optics Systems IV*, **9148**, 91481G, International Society for Optics and Photonics (2014).
- 38 B. Siquin, L. Prengere, C. Kulcsár, *et al.*, “On-sky results for adaptive optics control with data-driven models on low-order modes,” *MNRAS* **498**(3), 3228–3240 (2020). Publisher: Oxford University Press.
- 39 C. Petit, J.-F. Sauvage, T. Fusco, *et al.*, “SPHERE eXtreme AO control scheme: final performance assessment and on sky validation of the first auto-tuned LQG based operational system,” in *Adaptive Optics Systems IV*, **9148**, 91480O, International Society for Optics and Photonics (2014).
- 40 L. A. Poyneer, D. W. Palmer, B. Macintosh, *et al.*, “Performance of the Gemini Planet Imager’s adaptive optics system,” *Applied Optics* **55**(2), 323–340 (2016). Publisher: Optical Society of America.
- 41 C. M. Correia, C. Z. Bond, J.-F. Sauvage, *et al.*, “Modeling astronomical adaptive optics performance with temporally filtered Wiener reconstruction of slope data,” *JOSAA* **34**, 1877 (2017).
- 42 J. R. Males and O. Guyon, “Ground-based adaptive optics coronagraphic performance under closed-loop predictive control,” *JATIS* **4**, 1 (2018).
- 43 R. Ragazzoni and J. Farinato, “Sensitivity of a pyramidal Wave Front sensor in closed loop Adaptive Optics,” *A&A* **350**, L23–L26 (1999).
- 44 R. Juvénal, C. Kulcsár, H.-F. Raynaud, *et al.*, “Linear controller error budget assessment for classical adaptive optics systems,” *Journal of the Optical Society of America A* **35**, 1465 (2018).

- 45 J. M. Conan, G. Rousset, and P. Y. Madec, “Wave-front temporal spectra in high-resolution imaging through turbulence.,” *JOSAA* **12**, 1559–1570 (1995).
- 46 C. Vérinaud, “On the nature of the measurements provided by a pyramid wave-front sensor,” *Optics Communications* **233**, 27–38 (2004).
- 47 T. Fusco, J.-F. Sauvage, C. Petit, *et al.*, “Final performance and lesson-learned of SAXO, the VLT-SPHERE extreme AO: from early design to on-sky results,” in *Society of Photo-Optical Instrumentation Engineers (SPIE) Conference Series*, *Society of Photo-Optical Instrumentation Engineers (SPIE) Conference Series* **9148**, 1 (2014).
- 48 P.-Y. Madec, R. Arsenault, H. Kuntschner, *et al.*, “Adaptive Optics Facility: from an amazing present to a brilliant future...,” in *Adaptive Optics Systems VI*, L. M. Close, L. Schreiber, and D. Schmidt, Eds., **10703**, 1 – 13, International Society for Optics and Photonics, SPIE (2018).
- 49 G. Anglada-Escudé, P. J. Amado, J. Barnes, *et al.*, “A terrestrial planet candidate in a temperate orbit around Proxima Centauri,” *Nature* **536**, 437–440 (2016).
- 50 I. Ribas, M. Tuomi, A. Reiners, *et al.*, “A candidate super-Earth planet orbiting near the snow line of Barnard’s star,” *Nature* **563**, 365–368 (2018).
- 51 R. F. Díaz, X. Delfosse, M. J. Hobson, *et al.*, “The SOPHIE search for northern extrasolar planets. XIV. A temperate ($T_{\text{eq}} \sim 300$ K) super-earth around the nearby star Gliese 411,” *A&A* **625**, A17 (2019).
- 52 M. Zechmeister, S. Dreizler, I. Ribas, *et al.*, “The CARMENES search for exoplanets around M dwarfs. Two temperate Earth-mass planet candidates around Teegarden’s Star,” *A&A* **627**, A49 (2019).

- 53 A. Quirrenbach, P. J. Amado, I. Ribas, *et al.*, “CARMENES: high-resolution spectra and precise radial velocities in the red and infrared,” in *Ground-based and Airborne Instrumentation for Astronomy VII*, C. J. Evans, L. Simard, and H. Takami, Eds., *Society of Photo-Optical Instrumentation Engineers (SPIE) Conference Series* **10702**, 107020W (2018).
- 54 F. Wildi, N. Blind, V. Reshetov, *et al.*, “NIRPS: an adaptive-optics assisted radial velocity spectrograph to chase exoplanets around M-stars,” in *Society of Photo-Optical Instrumentation Engineers (SPIE) Conference Series*, *Society of Photo-Optical Instrumentation Engineers (SPIE) Conference Series* **10400**, 1040018 (2017).
- 55 R. Conan and C. Correia, “Object-oriented Matlab adaptive optics toolbox,” in *Adaptive optics systems IV*, **9148**, 91486C, International Society for Optics and Photonics (2014).
- 56 E. Gendron and P. Lena, “Astronomical adaptive optics. I. Modal control optimization.,” *A&A* **291**, 337–347 (1994).
- 57 V. Korkiakoski, C. Véraud, and M. Le Louarn, “Applying sensitivity compensation for pyramid wavefront sensor in different conditions,” in *Adaptive Optics Systems*, N. Hubin, C. E. Max, and P. L. Wizinowich, Eds., *Society of Photo-Optical Instrumentation Engineers (SPIE) Conference Series* **7015**, 701554 (2008).
- 58 V. Deo, E. Gendron, G. Rousset, *et al.*, “A modal approach to optical gain compensation for the pyramid wavefront sensor,” in *Adaptive Optics Systems VI*, L. M. Close, L. Schreiber, and D. Schmidt, Eds., **10703**, 653 – 670, SPIE (2018). Backup Publisher: International Society for Optics and Photonics.
- 59 C. Cavarroc, A. Boccaletti, P. Baudoz, *et al.*, “Fundamental limitations on Earth-like planet detection with extremely large telescopes,” *A&A* **447**, 397–403 (2006).

- 60 Cantalloube, F., Farley, O. J. D., Milli, J., *et al.*, “Wind-driven halo in high-contrast images - I. Analysis of the focal-plane images of SPHERE,” *A&A* **638**, A98 (2020).
- 61 C. Lovis, I. Snellen, D. Mouillet, *et al.*, “Atmospheric characterization of Proxima b by coupling the SPHERE high-contrast imager to the ESPRESSO spectrograph,” *A&A* **599**, A16 (2017).
- 62 C. Vérinaud, M. Le Louarn, V. Korkiakoski, *et al.*, “Adaptive optics for high-contrast imaging: pyramid sensor versus spatially filtered Shack-Hartmann sensor,” *MNRAS* **357**, L26–L30 (2005).
- 63 F. J. Rigaut, J.-P. Veran, and O. Lai, “Analytical model for Shack-Hartmann-based adaptive optics systems,” in *Adaptive Optical System Technologies*, D. Bonaccini and R. K. Tyson, Eds., *Society of Photo-Optical Instrumentation Engineers (SPIE) Conference Series* **3353**, 1038–1048 (1998).
- 64 D. L. Fried, “Time-delay-induced mean-square error in adaptive optics,” *J. Opt. Soc. Am. A* **7**, 1224–1225 (1990).
- 65 J. Hardy, *Adaptive Optics for Astronomical Telescopes*, Oxford series in optical and imaging sciences, Oxford University Press (1998).
- 66 C. Marois, R. Doyon, D. Nadeau, *et al.*, “Effects of Quasi-Static Aberrations in Faint Companion Searches,” *EAS Publications Series* **8**, 233–243 (2003).
- 67 J. Milli, D. Mawet, D. Mouillet, *et al.*, “Adaptive optics in high-contrast imaging,” *arXiv:1701.00836 [astro-ph]* **439**, 17–41 (2016). arXiv: 1701.00836.
- 68 S. B. Goebel, O. Guyon, D. N. B. Hall, *et al.*, “Measurements of Speckle Lifetimes in Near-

- infrared Extreme Adaptive Optics Images for Optimizing Focal Plane Wavefront Control,” *PASP* **130**, 104502 (2018).
- 69 B. Macintosh, L. Poyneer, A. Sivaramakrishnan, *et al.*, “Speckle lifetimes in high-contrast adaptive optics,” in *Astronomical Adaptive Optics Systems and Applications II*, R. K. Tyson and M. Lloyd-Hart, Eds., **5903**, 170 – 177, International Society for Optics and Photonics, SPIE (2005).
- 70 J. Milli, T. Banas, D. Mouillet, *et al.*, “Speckle lifetime in XAO coronagraphic images: temporal evolution of SPHERE coronagraphic images,” in *Adaptive Optics Systems V*, E. Marchetti, L. M. Close, and J.-P. Véran, Eds., **9909**, 1455 – 1472, International Society for Optics and Photonics, SPIE (2016).
- 71 D. Mawet, C. Z. Bond, J. R. Delorme, *et al.*, “Keck Planet Imager and Characterizer: status update,” in *Adaptive Optics Systems VI*, L. M. Close, L. Schreiber, and D. Schmidt, Eds., *Society of Photo-Optical Instrumentation Engineers (SPIE) Conference Series* **10703**, 1070306 (2018).
- 72 J. R. Males, L. M. Close, O. Guyon, *et al.*, “MagAO-X first light,” in *Society of Photo-Optical Instrumentation Engineers (SPIE) Conference Series*, *Society of Photo-Optical Instrumentation Engineers (SPIE) Conference Series* **11448**, 114484L (2020).

List of Figures

- 1 Two-stage CAO system architecture

- 2 Illustration of spectrum periodization for an input sinusoidal signal at $f_0 = 40$ Hz (left) and of aliasing and periodization for an input sinusoidal signal at $f_0 = 940$ Hz (right). Loop frequencies are $F_1 = 1$ kHz and $F_2 = 4$ kHz. The red lines correspond to the theoretical calculations, the blue circles to the empirical power spectral density computed from the simulation data by non-averaged periodogram. The y-axis is in arbitrary units.
- 3 For an input sinusoidal signal of amplitude 1 at $f_0 = 40$ Hz: inter-sampling signal ϕ^{is} (dotted orange), residual $\bar{\phi}^{\text{res},1}$ (plain grey), 1st stage output $\phi^{\text{res},1}$ (dotted-dashed blue) and 2nd stage residual signal $\phi^{\text{res},2}$ (plain red). Loop frequencies are $F_1 = 1$ kHz and $F_2 = 4$ kHz. The y-axis is in arbitrary units.
- 4 RTFs over the frequency range $[0, F_2/2]$. The signal $\bar{\phi}^{\text{tur}}$ generated at $F_1 = 1$ kHz and upsampled at $F_2 = 4$ kHz is rejected by $R_1 \times R_2$, while the inter-sampling signal ϕ^{is} is only rejected by R_2 . The double integrator RTF at $F_2 = 4$ kHz is in black. The y-axis is in arbitrary units.
- 5 Theoretical PSDs: on the left, schematic input PSD corresponding to a Zernike radial order $n_{\text{rad}}=3$, with cut-off frequency $f_c = 1.5$ Hz (plain blue), residual PSD $S_{\text{res},2}$ at the output of the 2-stage CAO system with loop frequency $F_2 = 4$ kHz (dotted red) and residual PSD with a double integrator at $F_2 = 4$ kHz (black). On the right, from top to bottom: input PSD (light blue), PSD of residual signal $\bar{\phi}^{\text{res},1}$ at the output of 1st stage with loop frequency $F_1 = 1$ kHz (dashed magenta), inter-sampling signal ϕ^{is} PSD (thick green) and PSD of the residual inter-sampling signal after rejection by the 2nd stage RTF R_2 (dotted dark blue).

- 6 Transfer functions. On (a), RTFs with best tuning for each regulator: double integrator (Dashed black line), 1st stage (blue line), 2nd stage (dotted red line). On (b), noise propagation transfer functions: double integrator (dashed black line), 1st stage (blue line), 2nd stage (red dotted line), 1st stage noise propagation rejected by 2nd stage (yellow dashed line).
- 7 PSDs in presence of a measurement noise variance of 410^{-4} [arb. units]: schematic modal input PSD (grey), input of the 2nd stage including inter-sampling signal (dotted blue), residual at the output of the CAO (plain red and dashed-dotted red for the case without noise), residual for the double integrator (dashed-dotted black and dotted yellow for the case without noise). The peaks of the 2nd stage input are at the same level than that of the CAO.
- 8 Wavefront error [nm] for different split-ratios (gray beam-splitter case) and magnitude. On the left side, the simulation were done using $r_0 = 0.1$ [m] and on the right side $r_0 = 0.157$ [m]. The darker the color, the bigger the WFE. In terms of RMS, the best overall performance is achieved using an 80%/20% split ratio for magnitudes up to 8 in I-band.
- 9 Residual WFE as a function of close loop gain and three different magnitudes.
- 10 Optical gains for the 2nd stage PWFS as a function of the Karhunen-Loève modes for two different values of the Fried parameter r_0 .

- 11 RMS in nanometers in terms of magnitude for the 1st stage only (solid blue line) and with the 2nd stage (dashed orange line) for (a) $r_0 = 0.1$ and (b) $r_0 = 0.157$. In the case where both wavefront sensors work on the I-band, the full flux is divided in a 80%/20% split ratio between both stages (circle markers). In the other case, the flux is divided in different wavelengths for each stage, and 100% of the flux is sent (cross markers).
- 12 Contrast performance and PSF for $r_0 = 0.1$ (a) and $r_0 = 0.157$ (b). Both stages operate their WFS in I-band, and the optimum gray beamsplitting ratio (80%/20%) was used. Scientific analysis is done in I-band as well.
- 13 Contrast performance and PSF for $r_0 = 0.1$ (a) and $r_0 = 0.157$ (b) and dichroic beamsplitting. All the J-Band flux was sent to the 1st stage, and all the I-band flux was sent to the 2nd stage. Scientific analysis is done in I-band.
- 14 PSF residual contrast as a function of magnitude at an angular separations of 40 mas.
- 15 Long exposure perfect coronagraph PSF with different regions A over imposed
- 16 Temporal decorrelations of all the pixels inside A for three different regions

List of Tables

- 1 System Parameters